

Uncertainty Quantification of GEOS-5 L-Band Radiative Transfer Model Parameters using Bayesian Inference and SMOS Observations

Gabriëlle J. M. De Lannoy^{a,b}, Rolf H. Reichle^a, Jasper A. Vrugt^{c,d,e}

^a*NASA Goddard Space Flight Center, Code 610.1, Greenbelt, MD 20771, USA*

^b*GESTAR, Universities Space Research Association, Columbia, MD 21044, USA*

^c*University of California, Irvine, Department of Civil and Environmental Engineering,
Irvine, CA 92697-2175, USA*

^d*University of California, Irvine, Department of Earth System Science, Irvine, CA
92697-2175, USA*

^e*Institute for Biodiversity and Ecosystems Dynamics, University of Amsterdam, 1098
XH Amsterdam, The Netherlands*

Abstract

Uncertainties in L-band (1.4 GHz) radiative transfer modeling (RTM) affect the simulation of brightness temperatures (Tb) over land and the inversion of satellite-observed Tb into soil moisture retrievals. In particular, accurate estimates of the microwave soil roughness, vegetation opacity and scattering albedo for large-scale applications are difficult to obtain from field studies and often lack an uncertainty estimate. Here, a Markov Chain Monte Carlo (MCMC) simulation method is used to determine satellite-scale estimates of RTM parameters and their posterior uncertainty by minimizing the misfit between long-term averages and standard deviations of simulated and observed Tb at a range of incidence angles, at horizontal and vertical polarization, and for morning and evening overpasses. Tb simulations are generated with the Goddard Earth Observing System (GEOS-5) and confronted with Tb observations from the Soil Moisture Ocean Salinity (SMOS)

1 mission. The MCMC algorithm suggests that the relative uncertainty of
2 the RTM parameter estimates is typically less than 25% of the maximum
3 a posteriori density (MAP) parameter value. Furthermore, the actual root-
4 mean-square-differences in long-term Tb averages and standard deviations
5 are found consistent with the respective estimated total simulation and obser-
6 vation error standard deviations of $\sigma_m=3.1$ K and $\sigma_s=2.4$ K. It is also shown
7 that the MAP parameter values estimated through MCMC simulation are
8 in close agreement with those obtained with Particle Swarm Optimization
9 (PSO).

10 *Keywords:*

11 radiative transfer modeling, brightness temperature, Bayesian parameter
12 estimation, uncertainty, Markov Chain Monte Carlo simulation, SMOS

1. Introduction

Uncertainties in radiative transfer modeling (RTM) affect the simulation of brightness temperatures (Tb) over land and the inversion of satellite-observed Tb to soil moisture retrievals. Quantification of these uncertainties is crucial to producing, validating and using passive microwave data, such as those obtained from the Soil Moisture Ocean Salinity (SMOS, Kerr et al. (2010)) and future Soil Moisture Active Passive (SMAP, Entekhabi et al. (2010)) missions. Yet, it is not particularly clear which RTM formulation and parameter values to use for large-scale applications.

In the context of forward Tb simulation, several studies have analyzed the effect of different RTM formulations for the microwave roughness length, vegetation parameterization and soil dielectric model (Drusch et al., 2009; de Rosnay et al., 2009). The impact of parameter values and dynamic land surface variables as input to large-scale forward Tb simulations was demonstrated by, e.g., De Lannoy et al. (2013) and Balsamo et al. (2006), respectively. Similarly, soil moisture retrievals based on Tb observations are affected by the RTM formulation and parameter values (Crosson et al., 2005; Panciera et al., 2009; Konings et al., 2011; Parinussa et al., 2011), as well as by the choice of background and auxiliary fields, such as soil temperature and vegetation characteristics (Kerr et al., 2012; O'Neill et al., 2012). Collectively, these studies suggest that RTMs exhibit significant uncertainty and that the precise magnitude and impact of this uncertainty on large-scale Tb simulations and soil moisture retrievals remain unclear.

Estimating the uncertainty of microwave RTM parameters is a major challenge, especially at larger spatial scales. Field experiments have pro-

1 vided RTM parameters values (de Rosnay et al., 2006; Grant et al., 2007;
 2 Panciera et al., 2009; Sabater et al., 2011), but mostly without uncertainty
 3 estimates. De Lannoy et al. (2013) derived global-scale RTM parameter val-
 4 ues and ad hoc uncertainty estimates using SMOS observations and Particle
 5 Swarm Optimization (PSO, Kennedy and Eberhart (1995)). PSO is espe-
 6 cially designed to find the optimal parameter values within a limited budget
 7 of function evaluations, but without recourse to estimating their underlying
 8 uncertainty.

9 In this paper, we introduce a (Bayesian) Markov chain Monte Carlo
 10 (MCMC) simulation method to estimate the posterior RTM parameter dis-
 11 tribution. The Differential Evolution Adaptive Metropolis (DREAM) algo-
 12 rithm is used with parallel direction and snooker sampling from past states
 13 (Vrugt et al., 2008, 2009; Laloy and Vrugt, 2012), referred to as DREAM_(ZS).
 14 Bayesian approaches such as DREAM_(ZS) have many advantages over op-
 15 timization methods such as PSO. The explicit treatment and analysis of
 16 uncertainty help to understand which parts of the RTM model are well re-
 17 solved and which elements require further attention. Furthermore, a formal
 18 analysis of the residuals can be used to check the validity of our assump-
 19 tions about the residual error distributions and to discern whether reliable
 20 parameter values have been derived.

21 The added value of obtaining posterior parameter distributions with Bayesian
 22 approaches, however, comes at an increased computational cost. Adequately
 23 sampling the posterior parameter distributions is too costly for global-scale
 24 operational applications that rely on evolving modeling systems in need of
 25 frequent re-calibrations, but can provide a valuable benchmark to verify re-

1 sults from simple parameter optimization algorithms, such as for example
2 PSO.

3 The goals of the present paper are thus to infer RTM parameters and
4 their posterior uncertainty using a Bayesian method, and to study the as-
5 sociated simulated Tb uncertainty. We are using the Goddard Earth Ob-
6 serving System (GEOS-5) modeling framework that will be used to gener-
7 ate the planned global SMAP Level 4 Surface and Root Zone Soil Moisture
8 (L4_SM) data product through assimilation of SMAP Tb observations (Re-
9 ichle et al., 2012). As in De Lannoy et al. (2013), we focus on optimizing
10 time-invariant RTM-parameters by minimizing climatological differences be-
11 tween multi-angular, horizontally and vertically polarized Tb for morning
12 and evening overpasses from SMOS observations and GEOS-5 simulations.
13 The time-invariant optimized parameters will later be used in a data assimi-
14 lation system (outside the scope of this paper), where state variables such as
15 soil moisture and soil temperature will be updated in response to short-term
16 variations in the observed Tb.

17 To summarize, in this paper we apply MCMC simulation using multi-
18 angular SMOS Tb observations to (i) verify if the maximum a posteriori
19 density (MAP) parameter values derived from a converged posterior distri-
20 bution with DREAM_(ZS) can be approximated using PSO, (ii) obtain reliable
21 parameter uncertainty estimates, and (iii) quantify the magnitude of param-
22 eter and other error sources in Tb simulations. The remainder of this paper
23 is organized as follows. Section 2 summarizes the modeling system and the
24 SMOS observations used in the present study. This is followed in section 3
25 by a description of the DREAM_(ZS) MCMC simulation method and PSO.

1 Section 3 also discusses several quantitative diagnostic metrics to analyze
 2 the simulated Tb uncertainty. Finally, this paper concludes in sections 4 and
 3 5 with a discussion of the results and conclusions.

4 **2. Observations and Model**

5 *2.1. SMOS Tb Data*

6 Since its launch in November 2009, the SMOS mission provides global Tb
 7 data at a nominal spatial resolution of 43 km and with an equator overpass
 8 every 3 days. Here we use the multi-angular, full polarization Tb data from
 9 the period 1 July 2010 to 1 July 2012. Specifically, the data are extracted
 10 from the MIR_SCLF1C product, with processor version 504 for the years 2010
 11 and 2011, and version 551 from January 2012 onwards. Our previous study
 12 presented in De Lannoy et al. (2013) discusses in detail the various steps
 13 involved in the processing of the SMOS data. Most importantly, the data
 14 are screened extensively using both product-based data quality information
 15 and model-based quality control rules. Furthermore, the data are spatially
 16 mapped onto a 36 km Equal-Area Scalable Earth Grid (EASE) and binned
 17 per incidence angle. Consistent with our previous study, only a subset of
 18 6 incidence angles is used: $\theta=[32.5^\circ, 37.5^\circ, 42.5^\circ, 47.5^\circ, 52.5^\circ, \text{ and } 57.5^\circ]$,
 19 where, for example, 32.5° represents the average of all data with incidence
 20 angles between 32° and 33° .

21 For the purpose of estimating the microwave RTM parameters, long-term
 22 averages (\mathbf{m}_o) and standard deviations (\mathbf{s}_o) of the SMOS data are computed
 23 separately for each of the 6 incidence angles, 2 polarizations (horizontal H
 24 and vertical V), and 2 overpass times (ascending at 06:00h local time (LT),

1 descending at 18:00h LT). This results in a total of 48 “observations” per grid
2 cell: 24 for the long-term average Tb and 24 for the long-term Tb standard
3 deviation. Section 3 provides more details.

4 2.2. GEOS-5 Tb Modeling

5 The modeling combines (i) land surface modeling with the Catchment
6 land surface model (CLSM) and (ii) radiative transfer modeling with a tau-
7 omega model to simulate long-term Tb averages and standard deviations. As
8 in De Lannoy et al. (2013), the GEOS-5 CLSM (Koster et al., 2000) is set up
9 on the 36 km EASE grid and spun up prior to the SMOS observation period.
10 Surface meteorological forcing data at a $1/2^\circ \times 2/3^\circ$ spatial and hourly tem-
11 poral resolution are taken from the Modern-Era Retrospective analysis for
12 Research and Applications (MERRA, Rienecker et al. (2011)). The MERRA-
13 precipitation is corrected with gauge-based precipitation from the National
14 Oceanic and Atmospheric Administration (NOAA) Climate Prediction Cen-
15 ter “Unified” (CPCU) product (Reichle, 2012). The model version is the
16 same as that used for the MERRA-Land data product (Reichle et al., 2011),
17 except for two changes that more closely align the model with the version
18 that will ultimately be used for the SMAP L4_LSM data product: (i) the sur-
19 face soil moisture pertains to the top 5 cm surface layer (as opposed to the
20 top 2 cm layer in MERRA-Land), and (ii) a preliminary version of updated
21 soil parameters from a forthcoming version of GEOS-5 is used.

22 The vegetation parameterization in CLSM uses 8 default vegetation classes.
23 For the RTM simulations, these classes are further refined into the 16 classes
24 defined by the Moderate Resolution Imaging Spectroradiometer (500 m MOD12Q1
25 V004) International Geosphere-Biosphere Programme (IGBP) land cover

1 classification (Loveland and Belward, 1997). Figure 1 shows the North Amer-
2 ican study domain which covers 9 of the 16 IGBP vegetation classes.

3 The soil moisture, soil temperature, vegetation water content, air temper-
4 ature and climatological vegetation dynamics simulated with the prognostic
5 CLSM are used as input to the diagnostic zero-order (tau-omega) microwave
6 RTM to simulate L-band Tb. A short description of the RTM is given in Ap-
7 pendix. In essence, the Tb is determined by the surface soil temperature and
8 attenuated by dynamic and static soil and vegetation characteristics. The
9 key model parameters that impact the rough surface reflectivity h (Eq. A.3,
10 Eq. A.4), the scattering albedo ω , and vegetation optical depth τ (Eq. A.6)
11 will be estimated using the multi-angular SMOS observations (section 3),
12 where h is a function of soil moisture and τ depends on the leaf area index
13 (LAI).

14 **3. Methods**

15 *3.1. Overview*

16 Keeping up with our previous work (De Lannoy et al., 2013), the objec-
17 tive of the parameter estimation is to minimize the difference between long-
18 term (climatological) averages and standard deviations for multiple types of
19 SMOS-observed and GEOS-5-modeled Tb. We purposely do *not* minimize
20 differences in the time domain as the goal of the present paper is to derive
21 parameter estimates that result in the smallest possible bias in the long-term
22 simulation of Tb. Short-term differences between Tb observations and simu-
23 lations will be exploited in future studies using sequential data assimilation.
24 We estimate a time-invariant multi-dimensional parameter set (hereafter re-

ferred to as α) that determines climatological features of the simulated Tb.
The parameters are optimized locally, i.e., for each grid cell independently,
and only for non-frozen land surface conditions as determined by the GEOS-5
modeling system.

Table 1 gives an overview of the parameters estimated in different experiments.
All scenarios estimate the 5 most relevant RTM-parameters: h_{min} ,
 $\Delta h \equiv h_{max} - h_{min}$, b_H , $\Delta b \equiv b_V - b_H$ and ω (according to the best scenario
identified in De Lannoy et al. (2013)). Based on these *time-invariant* parameters,
time-variant values of h , τ_H and τ_V are computed, using dynamic
information about soil moisture for h (Eq. A.4) and LAI for τ (Eq. A.6).
Time-averaged results for $\langle h \rangle$ and $\langle \tau \rangle$ are then presented, where $\langle \cdot \rangle$
denotes the long-term time average. These RTM-parameters are estimated
with either DREAM_(ZS) or PSO, hereafter referred to as scenarios D and P,
respectively. The DREAM_(ZS) analysis is further expanded to also include
the residual Tb error statistics σ_m and σ_s (scenario D _{σ} , discussed below).
For each grid cell, we thus estimate 5 parameters for scenarios P and D, and
7 for D _{σ} .

To derive these parameters, we minimize per grid cell the *climatological*,
or long-term, differences between 48 Tb observations and simulations. The
 2×24 observations consist of long-term Tb averages and Tb standard deviations
for the 24 combinations of 2 polarizations, 2 overpass times, and 6
incidence angles. The errors in these observations are assumed to be independent,
that is, we neglect correlations in instrument errors and errors between
H- and V-polarized observations at identical incidence angles. Similarly, the
simulation errors are assumed to be independent, even though correlation is

1 to be expected. Note that temporal correlations in the errors are of little
 2 concern because the observations are long-term averages and standard de-
 3 viations, and not measurements in the time domain (Wöhling and Vrugt,
 4 2011).

5 In keeping up with De Lannoy et al. (2013), the two years of historical
 6 SMOS data are divided into a calibration period (1 July 2011 - 1 July 2012)
 7 and an evaluation period (1 July 2010 - 1 July 2011). To ensure a meaningful
 8 calibration at each grid cell, we impose a minimum of 20 valid data points
 9 (N_i) per year to compute the long-term Tb average and standard deviation
 10 for a particular combination ($i = 1, \dots, 24$) of incidence angle, polarization
 11 and overpass time. The requirement of $N_i \geq 20$ is used for the calculation of
 12 evaluation statistics as well.

13 3.2. Markov Chain Monte Carlo (MCMC) Sampling

14 The Bayesian framework allows deriving posterior probabilities of param-
 15 eter estimates and model simulations, conditioned on errors in observations
 16 and simulations. The posterior probability distribution is computed by com-
 17 bining the observation likelihood $p(\mathbf{m}_o, \mathbf{s}_o | \boldsymbol{\alpha})$ with a prior distribution $p(\boldsymbol{\alpha})$:

$$p(\boldsymbol{\alpha} | \mathbf{m}_o, \mathbf{s}_o) = \frac{p(\mathbf{m}_o, \mathbf{s}_o | \boldsymbol{\alpha})p(\boldsymbol{\alpha})}{\int_{\boldsymbol{\alpha}} p(\mathbf{m}_o, \mathbf{s}_o | \boldsymbol{\alpha})d\boldsymbol{\alpha}} \quad (1)$$

18 The observations consist of long-term averages ($m_{i,o} \in \mathbf{m}_o$) and standard
 19 deviations ($s_{i,o} \in \mathbf{s}_o$) of Tb for 24 different combinations of incidence angles,
 20 polarizations and overpass times ($i = 1, \dots, 24$). The denominator is a nor-
 21 malization factor and thus it suffices to maximize $p(\mathbf{m}_o, \mathbf{s}_o | \boldsymbol{\alpha})p(\boldsymbol{\alpha})$ to find
 22 the posterior distribution of $\boldsymbol{\alpha}$. In practice, it is difficult to solve this prob-
 23 lem analytically and we therefore resort to MCMC simulation to generate a

1 sample of the posterior target distribution.

2 In this paper, the differential evolution adaptive metropolis (DREAM_(ZS),
3 Vrugt et al. (2008); Laloy and Vrugt (2012)) algorithm with sampling from
4 past states is used to efficiently explore the posterior parameter distribution.
5 This algorithm adaptively updates the scale and orientation of the proposal
6 distribution during sampling, and is specifically designed to rapidly explore
7 multi-dimensional target distributions. In DREAM_(ZS), multiple chains are
8 running in parallel and the update of a chain is determined from an external
9 sample of points that collectively summarizes the search history of all the
10 individual chains. The log-likelihood of the current and proposed parameter
11 values are compared using the Metropolis selection rule. If the proposal is
12 accepted, the chain moves to this new point, otherwise the chain remains
13 at its current position. Diminishing adaptation of the external archive of
14 samples ensures convergence to the exact posterior distribution.

15 We assume a Gaussian prior for each of the individual parameters $\alpha_{0,k} \in$
16 $\boldsymbol{\alpha}_0$. The mean and standard deviation of this multi-normal distribution $p(\boldsymbol{\alpha})$
17 are derived from literature values that yield reasonable Tb simulations com-
18 pared to SMOS Tb and are summarized in Table 1. Note that these values
19 were referenced as ‘Lit2’ in De Lannoy et al. (2013). The prior mean for each
20 individual parameter is given by a vegetation-dependent value $\alpha_{0,k}$ and the
21 standard deviation $\sigma_{\alpha_{0,k}}$ is defined by $\sigma_{\alpha_{0,k}}^2 = (\alpha_{max,k} - \alpha_{min,k})^2/12$, using
22 upper and lower bounds $[\alpha_{max,k}, \alpha_{min,k}]$.

23 The following log-likelihood function is used to minimize the differences in
24 long-term Tb averages and standard deviations between observations $(m_{i,o}, s_{i,o})$

1 and simulations ($m_i(\boldsymbol{\alpha}), s_i(\boldsymbol{\alpha})$):

$$\begin{aligned}
L = \ln(p(\mathbf{m}_o, \mathbf{s}_o | \boldsymbol{\alpha})) = & -\frac{24}{2} \ln(2\pi) - \frac{24}{2} \ln(\sigma_{i,m}^2) - \sum_{i=1}^{24} \frac{(m_{i,o} - m_i(\boldsymbol{\alpha}))^2}{2\sigma_{i,m}^2} \Bigg\} L_{m,o} \\
& - \frac{24}{2} \ln(2\pi) - \frac{24}{2} \ln(\sigma_{i,s}^2) - \sum_{i=1}^{24} \frac{(s_{i,o} - s_i(\boldsymbol{\alpha}))^2}{2\sigma_{i,s}^2} \Bigg\} L_{s,o} \quad (2)
\end{aligned}$$

2 This formulation thus explicitly takes into consideration long-term biases in
3 the Tb average ($L_{m,o}$ [-]) and the Tb variability ($L_{s,o}$ [-]) and is derived from
4 a classical Gaussian likelihood function:

$$\begin{aligned}
p(\mathbf{m}_o, \mathbf{s}_o | \boldsymbol{\alpha}) = & \prod_{i=1}^{24} \left[\frac{1}{\sqrt{2\pi\sigma_{i,m}^2}} \exp \left(-\frac{(m_{i,o} - m_i(\boldsymbol{\alpha}))^2}{2\sigma_{i,m}^2} \right) \right] \\
& \cdot \prod_{i=1}^{24} \left[\frac{1}{\sqrt{2\pi\sigma_{i,s}^2}} \exp \left(-\frac{(s_{i,o} - s_i(\boldsymbol{\alpha}))^2}{2\sigma_{i,s}^2} \right) \right] \quad (3)
\end{aligned}$$

5 where $\sigma_{i,m}$ and $\sigma_{i,s}$ denote the (ensemble) standard deviations of the residual
6 differences between the observed and simulated values of the long-term Tb
7 averages and standard deviations, respectively.

8 3.3. Particle Swarm Optimization (PSO)

9 The PSO algorithm (Kennedy and Eberhart, 1995) is a global search
10 method that uses a dynamic swarm of particles to explore the parameter
11 space. The best position of each individual particle (cognitive aspect) and
12 of the entire swarm (social aspect) are used to guide the particles towards
13 the optimal solution. The iterative swarm search is performed in several
14 independent repetitions to account for sampling variability.

15 The fitness of each parameter combination in the swarm is measured by
16 an integrated ‘cost’ or ‘objective function’ J [-] that measures the distances

1 between the observed and simulated long-term Tb averages ($J_{m,o}$ [-]) and
 2 standard deviations ($J_{s,o}$ [-]). To make sure that the estimated parameter
 3 values honor the prior information (as used in DREAM_(ZS)), we also include
 4 a penalty term that quantifies deviations of the parameters from their ex-
 5 pected values (J_α [-]). This results in the following definition of the objective
 6 function to be minimized:

$$\begin{aligned}
 J = & \left\{ \sum_{i=1}^{24} \frac{(m_{i,o} - m_i(\boldsymbol{\alpha}))^2}{2\sigma_{i,m}^2} \right\} J_{m,o} \\
 & + \left\{ \sum_{i=1}^{24} \frac{(s_{i,o} - s_i(\boldsymbol{\alpha}))^2}{2\sigma_{i,s}^2} \right\} J_{s,o} \\
 & + \left\{ \sum_{k=1}^{N_\alpha} \frac{(\alpha_{0,k} - \alpha_k)^2}{2\sigma_{\alpha_{0,k}}^2} \right\} J_\alpha
 \end{aligned} \tag{4}$$

7 where N_α signifies the number of simultaneously estimated parameters. This
 8 formulation is essentially similar to the definition of the posterior density
 9 used in DREAM_(ZS). The main difference is that PSO handles the prior
 10 information of the parameters explicitly as penalty term J_α in the objective
 11 function, whereas in DREAM_(ZS), the prior parameter distribution is handled
 12 independently from the likelihood function by application of Bayes law. Both
 13 methods should thus find the same “best” parameter values.

14 3.4. Likelihood, Objective Function and Algorithm Settings

15 The design of the likelihood (L) or objective (J) function for DREAM_(ZS)
 16 and PSO warrants further discussion. As discussed above, we sample the cli-
 17 matological, or long-term, Tb averages and standard deviations over multiple
 18 incidence angles, polarizations and overpass times (that is, 2×24 observa-
 19 tions, $i = 1, \dots, 24$) per location, rather than one observation at multiple

1 time steps. The long-term Tb averages and standard deviations could also
 2 be interpreted as ‘summary statistics’ or ‘signatures’ of the system, and hence
 3 our approach has many elements in common with the diagnostic model eval-
 4 uation procedure presented in Vrugt and Sadegh (2013).

5 The variables $\sigma_{i,m}$ and $\sigma_{i,s}$ in Eq. 2 and Eq. 4 measure the (ensemble)
 6 standard deviation of the residual differences between the observed and sim-
 7 ulated long-term Tb averages and standard deviations, respectively, for each
 8 observation i . The residual errors are assumed to have a zero mean and in-
 9 clude both SMOS observation and simulation errors, due to e.g. inaccurate
 10 soil moisture, temperature or vegetation characteristics. These $\sigma_{i,m}$ and $\sigma_{i,s}$
 11 statistics trade-off errors in the long-term Tb averages against those of the
 12 long-term Tb standard deviations (as well as deviations from the prior pa-
 13 rameter constraints). Since only one sample is available for each observation,
 14 it is impossible to estimate individual $\sigma_{i,m}$ - and $\sigma_{i,s}$ -values. Therefore, we de-
 15 fine $\sigma_{i,m}$ and $\sigma_{i,s}$ as a combination of a homoscedastic term (σ_m, σ_s) and a
 16 tuning factor w_i to account for the robustness of the diagnosed long-term Tb
 17 averages and standard deviations, i.e. $\sigma_{i,m}^2 = w_i \sigma_m^2$ and $\sigma_{i,s}^2 = w_i \sigma_s^2$. The
 18 homoscedastic term is identical for all 24 observations and set to a default
 19 value of 1 K (De Lannoy et al., 2013), or alternatively we estimate σ_m and σ_s
 20 jointly with the RTM parameters (see section 3). The weights are given by
 21 $w_i = \frac{N}{N_i}$, where N_i denotes the number of data points in time that contribute
 22 to a particular long-term Tb average (or standard deviation), and N signifies
 23 the average number of time steps across all observations. These weights are
 24 typically close to 1 and assign somewhat more (less) weight to climatologi-
 25 cal differences that are based on more (fewer) individual data points in the

1 original 1-year data time series.

2 A maximum of 12,000 log-likelihood function evaluations are performed
 3 with DREAM_(ZS) using standard settings of the algorithmic variables. For
 4 PSO, we use the same algorithmic settings as De Lannoy et al. (2013), except
 5 a swarm size of 10 particles is used with a minimum of 10 and maximum of 100
 6 iterations. The search is terminated if the reduction of the objective function
 7 is smaller than 1E-5 over the last 10 iterations. A total of 12 repetitions are
 8 performed, which results in a maximum of 12,000 function evaluations.

9 3.5. Posterior Parameter Distribution

10 The ‘optimal’ parameter values are defined as those with the maximal a
 11 posteriori density (MAP), i.e. with the largest value for L (Eq. 2, DREAM_(ZS))
 12 or smallest value for J (Eq. 4, PSO). Note that these MAP values are not nec-
 13 essarily identical to the posterior ensemble mean of the distribution derived
 14 with of DREAM_(ZS). For the DREAM_(ZS) experiments, the last 25% of the
 15 MCMC chains (3,000 samples) are used to summarize parameter uncertainty
 16 by calculating the standard deviation of each individual parameter. To illus-
 17 trate this in more detail for one grid cell, consider Fig. 2a, which depicts the
 18 marginal distributions of the RTM parameters. We define the uncertainty as
 19 the ensemble standard deviation $stdv[\alpha] \equiv \overline{\alpha - \bar{\alpha}}$ centralized around the en-
 20 semble mean $\bar{\alpha}$, not around the MAP parameter value α_{MAP} . The notation
 21 $\overline{\cdot}$ refers to the ensemble mean. Note that the standard deviation around
 22 the MAP estimate $stdv_{MAP}[\cdot]$ can be found as a function of the centralized
 23 standard deviation $stdv[\cdot]$, i.e. $stdv_{MAP}[\cdot]^2 = stdv[\cdot]^2 + \Delta_{\alpha}(\Delta_{\alpha} - stdv[\cdot])$,
 24 where $\Delta_{\alpha} = \bar{\alpha} - \alpha_{MAP}$ is the difference between the ensemble mean and
 25 MAP parameter estimate. We found that, across the different experiments,

1 Δ_α is either small or Δ_α and $stdv[.]$ are of similar magnitude (not shown
2 herein), so that $stdv_{MAP}[.] \sim stdv[.]$.

3 3.6. Convergence

4 ‘Convergence’ can reflect accuracy (closeness to the actual optimum solu-
5 tion) or precision (reduction of the prior uncertainty). The following hypothe-
6 ses will be verified to assess the convergence of the DREAM_(zs) algorithm:
7 (i) the Tb performance (accuracy) with posterior parameter estimates should
8 be better than with prior parameter guesses (section 3.7), (ii) the posterior
9 parameter uncertainty (section 3.5) and the corresponding uncertainty in Tb
10 simulations (section 3.7) should be reduced compared to their counterparts
11 derived from the prior parameter uncertainty, and (iii) the potential scale re-
12 duction factor \sqrt{R} by Gelman and Rubin (1992) should be near 1 to inspire
13 confidence that the different MCMC chains have converged to the appro-
14 priate limiting distribution. The latter metric measures by which scale the
15 posterior distribution will shrink as the number of MCMC iterations would
16 go to infinity.

17 3.7. Tb Performance and Ensemble Verification

18 A number of measures are used to evaluate the long-term Tb simulations
19 and their associated uncertainty. Fig. 2b illustrates some of the terms used
20 in this evaluation. First, we assess the quality of the deterministic Tb sim-
21 ulations with the MAP parameter estimates, using the mean-square differ-
22 ence (MSD [K^2]) between the observed and simulated long-term Tb averages

1 (Eq. 5) and standard deviations (Eq. 6) across the 24 different observations:

$$MSD_m = \frac{1}{24} \sum_{i=1}^{24} (m_i(\boldsymbol{\alpha}_{MAP}) - m_{i,o})^2 \quad (5)$$

$$MSD_s = \frac{1}{24} \sum_{i=1}^{24} (s_i(\boldsymbol{\alpha}_{MAP}) - s_{i,o})^2 \quad (6)$$

2 If the modeling errors were solely due to uncertainties in the parameter val-
 3 ues, these metrics should be very close to zero. In practice, however, the
 4 metrics will substantially deviate from zero and reflect residual errors that
 5 cannot be explained by parameter uncertainty. The 24 differences contribut-
 6 ing to MSD_m are illustrated as Δ_{m_i} in Fig. 2b.

7 Secondly, we verify whether the spread in prior and posterior ensemble Tb
 8 simulations is in agreement with the misfit between modeled and observed
 9 values, in a mean-square sense. To this end, an ensemble of Tb simulations
 10 is generated by randomly drawing 20 samples from the prior and posterior
 11 parameter distributions. The misfit or skill is again defined using the mean-
 12 square difference ($MSD [K^2]$), but now for the ensemble means:

$$MSD_{\overline{m}} = \frac{1}{24} \sum_{i=1}^{24} \left(\overline{m_i(\boldsymbol{\alpha})} - m_{i,o} \right)^2 \quad (7)$$

$$MSD_{\overline{s}} = \frac{1}{24} \sum_{i=1}^{24} \left(\overline{s_i(\boldsymbol{\alpha})} - s_{i,o} \right)^2 \quad (8)$$

13 where $\overline{\cdot}$ denotes the ensemble mean. Fig. 2b illustrates the 24 differences
 14 contributing to $MSD_{\overline{m}}$ as $\Delta_{\overline{m}_i}$. If the uncertainties are well estimated and
 15 biases between observations and simulations are constrained during the cal-
 16 ibration, the $MSD_{\overline{m}}$ and $MSD_{\overline{s}}$ metrics should match the total expected
 17 uncertainty ($MEnSp_m$, $MEnSp_s$), which is the sum of the Tb simulation

1 spread due to parameter uncertainty ($EnSp_{i,m,par}$, $EnSp_{i,s,par}$) plus the resid-
 2 ual Tb error variance ($\sigma_{i,m}^2$, $\sigma_{i,s}^2$):

$$MEnSp_m = \frac{1}{24} \sum_{i=1}^{24} [EnSp_{i,m,par} + \sigma_{i,m}^2] \quad (9)$$

$$MEnSp_s = \frac{1}{24} \sum_{i=1}^{24} [EnSp_{i,s,par} + \sigma_{i,s}^2] \quad (10)$$

3 where $\sigma_{i,m}^2$ and $\sigma_{i,s}^2$ are dominated by observation, input and structural error
 4 after the MAP parameters values have been found. The constituent terms
 5 $EnSp_{i,m,par}$ and $EnSp_{i,s,par}$ for each observation type i are given by:

$$EnSp_{i,m,par} = \overline{(m_i(\boldsymbol{\alpha}) - \overline{m_i(\boldsymbol{\alpha})})^2} \quad (11)$$

$$EnSp_{i,s,par} = \overline{(s_i(\boldsymbol{\alpha}) - \overline{s_i(\boldsymbol{\alpha})})^2} \quad (12)$$

6 An illustration of $EnSp_{i,m,par}$ is given in Fig. 2b. Again, if the uncertainties
 7 are well estimated, then the ratios $MSD_{\overline{m}}/MEnSp_m$ and $MSD_{\overline{s}}/MEnSp_s$
 8 should be close to 1, or in other words: the “actual” ($MSD_{\overline{m}}$, $MSD_{\overline{s}}$) and
 9 “expected” ($MEnSp_m$, $MEnSp_s$) errors should be similar. These metrics
 10 are very similar to those used to verify the prescribed observation and simu-
 11 lation uncertainties in data assimilation systems (Reichle et al., 2002) and for
 12 ensemble forecast verification (De Lannoy et al., 2006). The only difference
 13 is that here, the mean values (i.e. the ‘M’, or mean, in MSD and $MEnSp$)
 14 are derived from multiple observations types ($i = 1, \dots, 24$), whereas in the
 15 earlier studies the mean was calculated in the time domain.

1 4. Results

2 4.1. RTM-Parameters and Their Uncertainty

3 In this section, we analyze the MAP values of $\langle h \rangle$, $\langle \tau \rangle$ and ω , and
4 their posterior uncertainty ($stdv[.]$). The DREAM_(ZS) scenario D_σ should
5 be considered as benchmark in the following discussion, because of statisti-
6 cal rigor of the sampled posterior (will be further discussed below). Fig. 3
7 shows maps of the prior parameter values and the MAP estimates derived
8 from scenario P (PSO), D and D_σ (DREAM_(ZS)) (Table 1). The spatially
9 averaged posterior parameter values are very similar for all 3 scenarios, with
10 a microwave roughness $\langle h \rangle$ around 0.75 ± 0.5 [-], a nadir opacity $\langle \tau \rangle$
11 of 0.26 ± 0.15 [-] and a scattering albedo ω of 0.09 ± 0.07 [-], where the values
12 after the \pm sign measure the spatial standard deviation and reflect the vari-
13 ability of the MAP parameters across the spatial domain. Note that these
14 values should not be confused with uncertainty estimates. Compared to the
15 prior values (Table 1 and 2), $\langle h \rangle$ has generally increased for grassland,
16 $\langle \tau \rangle$ is smaller for forests and ω has increased for all vegetation classes
17 except grassland (details per vegetation class not shown; these finding are
18 similar to those of De Lannoy et al. (2013)). The spatial patterns for the 3
19 scenarios are also very similar. Moreover, Fig. 3 suggests that MAP values
20 derived with the PSO algorithm closely match those of DREAM_(ZS).

21 Fig. 4 shows the ensemble parameter uncertainty for scenarios D and D_σ .
22 Maps with RTM parameter uncertainty estimates for PSO (obtained as in
23 De Lannoy et al. (2013)) are not shown, because they are statistically invalid
24 and significantly larger than those derived with DREAM_(ZS). The relative
25 uncertainties for scenario D are less than 10% of the MAP parameter value

1 and substantially smaller than the spatial variability in the MAP values. For
 2 scenario D_σ , the relative uncertainties increase, with errors ranging up to
 3 25% of the MAP values: for $\langle h \rangle$, the spatially averaged uncertainty is
 4 0.10 ± 0.08 [-], for $\langle \tau \rangle$ 0.04 ± 0.04 [-] and for ω 0.02 ± 0.02 [-], respectively.
 5 The uncertainty in $\langle h \rangle$ typically increases with more complex terrain and is
 6 smallest in the cropped region southwest of the Great Lakes. The uncertainty
 7 of $\langle \tau \rangle$ is largest in the forested Appalachian mountains where the highest
 8 MAP values of $\langle \tau \rangle$ are found. On the contrary, ω is best defined in this
 9 area and uncertainties in ω increase in the Western dry mountain ranges. The
 10 $\langle h \rangle$ -values are more uncertain where either the uncertainty in ω (Fig. 4e)
 11 or $\langle \tau \rangle$ (Fig. 4f) is larger.

12 In summary, both DREAM_(ZS) scenarios D and D_σ provide MAP pa-
 13 rameter values that are very similar and in close agreement with the PSO
 14 estimates. The DREAM_(ZS) derived posterior parameters appear well defined
 15 with relative uncertainties that are less than 25% of the MAP values. It will
 16 be shown below that the uncertainty estimates of scenario D_σ are consistent
 17 with the sample RMSD between long-term Tb observations and simulations.

18 *4.2. Residual Tb Error Standard Deviation Estimation*

19 To analyze the effect of σ_m and σ_s in more detail, Table 2 summarizes the
 20 MAP parameter values and their associated uncertainties averaged over the
 21 entire study domain. In addition, Fig. 5 depicts the results for different veg-
 22 etation classes. As discussed above, scenarios D and D_σ return similar MAP
 23 RTM-parameter values, but when σ_m and σ_s are simultaneously estimated,
 24 the posterior RTM-parameter uncertainty increases about 2 - 3 times. The
 25 domain-averaged values for scenario D_σ are $\sigma_m = 3.1$ K and $\sigma_s = 2.4$ K

1 (Table 2), whereas scenario D uses default values of these variables of 1 K.

2 The value of σ_m and its posterior uncertainty are largest in cropped re-
3 gions (Fig. 5g) where residual Tb errors are dominated by less skillful model
4 simulations. This is to be expected because irrigation is not simulated and
5 the climatological LAI estimates do not account for interannual crop rota-
6 tions. The parameters can not compensate for these errors, and the default
7 values of $\sigma_m = \sigma_s = 1$ K make scenarios D and P vulnerable to suboptimal
8 solutions. For example, the relative large differences between D and D $_{\sigma}$ for
9 σ_m and σ_s over cropland areas increases the differences in the MAP values of
10 ω . For forests, $\sigma_s = 1$ K appears to be a good estimate (Fig. 5i) because the
11 variability in Tb is expected to be low due to vegetation attenuation. Both
12 the MAP values and uncertainties for σ_m are always larger than those derived
13 for σ_s . One of the reasons for the higher σ_m are the opposite signs in the
14 biases for the long-term averages of ascending and descending Tb, which can-
15 not be mitigated with time-invariant RTM-parameters. These biases are due
16 to sensor error and modeled temperature errors as discussed in De Lannoy
17 et al. (2013). In a separate exercise (not shown herein), we verified that the
18 σ -values absorb biases in geophysical fields: by re-scaling the soil moisture
19 both the *RMSD* (see below) and σ -values are jointly reduced.

20 For the simulations with prior parameters, we also calculated (i.e. not
21 optimized) σ_m and σ_s as 7.5 K and 4.8 K, respectively (Table 2). Unlike
22 the MAP σ_m - and σ_s -values, these prior residual σ -values are dominated by
23 simulation error due to suboptimal parameter values.

1 4.3. MAP Tb Performance

2 Fig. 6 shows the misfit between observed and MAP simulated long-term
3 Tb averages and standard deviations ($RMSD_m$, $RMSD_s$, square-root of
4 Eq. 5 and 6) across the 24 observations for the calibration and evaluation
5 period, averaged per vegetation class. The performance skill is very similar
6 for scenarios P, D and D_σ , which reflects that the three scenarios generate
7 similar parameter estimates. The $RMSD_m$ ranges between 2 and 4.5 K dur-
8 ing the calibration (Fig. 6a) and increases up to 8 K for cropland in the
9 evaluation period (Fig. 6c). The $RMSD_s$ ranges between 1 and 3 K during
10 calibration (Fig. 6b) and reaches values of 5 K for cropland in the evaluation
11 year (Fig. 6d). Cropland has the highest errors, because of known simula-
12 tion errors (see above). Note also that the $RMSD_m$ and $RMSD_s$ values of
13 scenario D_σ during the calibration period (Fig. 6a-b) show the same pattern
14 as σ_m and σ_s in Fig. 5g and 5i. The increased errors in the evaluation period
15 suggest that the calibration could benefit from climatological observations
16 based on longer data records to better estimate the parameter values.

17 4.4. Ensemble Tb Performance

18 For DREAM_(ZS), we analyze the balance between the actual Tb misfit and
19 the expected uncertainty (ensemble variance) in the ensemble Tb simulations
20 (20 members, as opposed to single deterministic MAP simulations above).
21 The results are presented in Table 2 and Fig. 7. Table 2 shows the skill of the
22 ensemble mean Tb simulations $\overline{m_i(\boldsymbol{\alpha})}$ and $\overline{s_i(\boldsymbol{\alpha})}$ for the calibration period in
23 terms of $RMSD_{\overline{m}}$ and $RMSD_{\overline{s}}$, i.e. the square-root of Eqs. 7 and 8. These
24 values are very similar to the results for the MAP simulations (section 4.3).
25 For both scenarios D and D_σ , the $RMSD_{\overline{m}}$ and $RMSD_{\overline{s}}$ are respectively

1 3 K and 2.5 K, which is less than half of the actual misfit when the prior
2 parameters are used.

3 Table 2 also lists the square-root of the combined mean simulation and
4 observation spread or expected uncertainty, i.e. $RMEnSp_m$ and $RMEnSp_s$
5 (square-root of Eqs. 9 and 10), along with the constituent terms ($RMEnSp_{m,par}$,
6 $RMEnSp_{s,par}$, σ_m and σ_s). Generally, the uncertainty associated with the
7 parameter values is much smaller than the uncertainty related to other fac-
8 tors, that is, $RMEnSp_{par} < \sigma$, which is valid both when using prior and
9 posterior parameter distributions. Moreover, after calibration both the σ -
10 and $RMEnSp_{par}$ -values are significantly reduced compared to their prior
11 values.

12 If the uncertainty estimates are consistent, $RMSD_{\overline{m}} \sim RMEnSp_m$ and
13 $RMSD_{\overline{s}} \sim RMEnSp_s$, i.e. there should be a balance between the actual and
14 expected errors (section 3.7). The domain-averaged $RMSD_{\overline{m}}/RMEnSp_m$ is
15 2.7 for scenario D and 1.0 for scenario D_σ . Similarly, the domain-averaged
16 $RMSD_{\overline{s}}/RMEnSp_s$ is 2.5 for scenario D and 1.0 for scenario D_σ . Optimal
17 results are thus only found after including an estimation of σ_m and σ_s in
18 scenario D_σ . Note that for the evaluation period (not shown), the ratios
19 always exceed 1, because of an increased $RMSD_{\overline{m}}$ and $RMSD_{\overline{s}}$.

20 Fig. 7 shows how the ensemble spread is consistent with misfits between
21 observations and simulations for scenario D_σ . Specifically, Fig. 7a shows the
22 SMOS observed $m_{i,o}$ and the GEOS-5 simulated $\overline{m_i(\boldsymbol{\alpha})}$ for ascending, H-
23 polarized Tb at 6 angles for scenarios D and D_σ , averaged over the entire
24 study domain. Fig. 7b shows the same for V-polarized Tb, and Figs. 7c
25 and d provide this information for the long-term Tb standard deviations.

Also shown is the total ensemble simulation and observation uncertainty for each observation type, presented as error bars around the ensemble mean Tb simulations for illustration.

The error-bars for scenario D_σ fully envelop the observations, whereas this is not the case for scenario D. Fig. 7 also explains the nature of the residual misfit. Except for the 57.5°-angle, the ascending ensemble mean simulations $\overline{m_i(\boldsymbol{\alpha})}$ consistently underestimate the SMOS-observed $m_{i,o}$ for H-polarization and randomly deviate from the SMOS-observed $m_{i,o}$ at V-polarization. In contrast, the descending simulations $\overline{m_i(\boldsymbol{\alpha})}$ slightly overestimate the SMOS-observed $m_{i,o}$ at H-polarization (see De Lannoy et al. (2013)). The SMOS-observed $s_{i,o}$ is always larger than the simulated $\overline{s_i(\boldsymbol{\alpha})}$. This is probably dominated by observation noise, but could also be attributed to an underestimated variability in the Tb simulations. For example, an increase in the RTM-parameter h not only compensates for a cold bias but simultaneously also reduces the Tb variability. Fig. 7 clearly illustrates why the uncertainty estimates obtained from scenario D_σ are superior.

4.5. Convergence and Computational Cost

The effectiveness of the posterior parameter sampling is measured by the convergence of the algorithms. Table 2 confirms that both the posterior uncertainties in the parameter estimates ($stdv[.]$) and the misfit between the simulations and observations ($RMSD$) of the long-term Tb averages and standard deviations are greatly reduced compared to the results with the prior parameter distribution. Another measure for convergence is the scale reduction factor, or \sqrt{R} -statistic by Gelman and Rubin (1992). Values close to 1 are preferred, and suggest that the MCMC sampler has converged to a

1 limiting distribution. Fig. 8 shows the evolution of the convergence diagnostic
2 \sqrt{R} for both DREAM_(ZS) scenarios. The \sqrt{R} is averaged over all estimated
3 parameters and across the study domain, since no obvious differences in \sqrt{R}
4 are found between the different vegetation classes (not shown). Initially, the
5 values of \sqrt{R} exhibit a lot of variation (due to random initial sample) before
6 they settle down and reach values close to 1.

7 Finally, we report that the derivation of the posterior distributions re-
8 quires approximately 225 seconds for a single grid cell using DREAM_(ZS).
9 For global applications that involve $10^5 - 10^6$ grid cells, posterior distribu-
10 tion exploration may be too costly. Yet, if we target the MAP value only,
11 PSO or DREAM_(ZS) are both viable options.

12 5. Conclusions

13 Accurate estimates of microwave RTM parameters for large-scale L-band
14 applications are difficult to obtain. The available parameter estimates are
15 generally based on small-scale field experiments and often come without any
16 estimate of posterior uncertainty. This complicates radiative transfer mod-
17 eling for both the forward simulation of L-band Tb over land and the re-
18 trieval of soil moisture based on Tb observations. This paper expands earlier
19 research reported in De Lannoy et al. (2013) to derive time-invariant RTM-
20 parameters using observations of the long-term average Tb and the long-term
21 Tb standard deviation obtained from SMOS data. The overall objective is to
22 optimize GEOS-5 Tb simulations prior to sequential assimilation of SMOS
23 or SMAP Tb data, such as planned for the SMAP L4_SM product (Reichle
24 et al., 2012) and to examine the uncertainties involved in the optimization.

1 Per grid cell, 48 observations of the long-term Tb averages and standard de-
2 viations were constructed for 24 different combinations of 6 incidence angles,
3 2 polarizations and 2 overpass times. The differences with their respective
4 long-term GEOS-5 simulations are minimized (as opposed to minimizing dif-
5 ferences between Tb observations and simulations in the time domain) and
6 used along with the prior parameter information to derive posterior param-
7 eter estimates.

8 In the present paper, the full posterior distribution of RTM-parameters
9 is derived using MCMC simulation with the DREAM_(ZS) algorithm. To our
10 knowledge, this is the first large-scale application of the DREAM_(ZS) algo-
11 rithm for the estimation of RTM-parameters and their underlying uncer-
12 tainty. The results serve as a benchmark to verify the results from simpler
13 parameter optimization algorithms, such as for example PSO. Simple algo-
14 rithms are desirable for global-scale operational applications that rely on
15 evolving modeling systems in need of frequent re-calibrations.

16 First, we verified that the MAP RTM-parameter values derived from
17 converged posterior distributions with DREAM_(ZS) can be approximated by
18 a simpler optimization algorithm (PSO), which corroborates our earlier re-
19 search (De Lannoy et al., 2013). Secondly, we obtained reliable parameter
20 uncertainty estimates with DREAM_(ZS), which are impossible to estimate
21 with PSO. The relative parameter uncertainties are generally less than 25%
22 of the MAP value for $\langle h \rangle$, $\langle \tau \rangle$ and ω , when including the residual
23 (observation and simulation) error statistics (σ_m , σ_s) of the long-term Tb
24 averages and standard deviations in the estimation.

25 The third objective of this paper was to quantify the importance of param-

eter and other errors on Tb simulations. The uncertainty associated with the
 parameter values only contributes a small part to the total Tb uncertainty.
 Most of the discrepancy between Tb simulations and observations is covered
 by residual Tb errors, with MAP estimates of the standard deviations σ_m and
 σ_s (assumed homoscedastic) around 3.1 K and 2.4 K, respectively. The prior
 estimate of 1 K was thus too low, except for σ_s over forests which exhibit
 limited Tb variability due to vegetation attenuation. The largest σ_m -values
 are found in cropped regions where the RMSD between Tb simulations and
 observations is also highest, due to observation errors and errors in geophys-
 ical fields (e.g. soil moisture and temperature) that constitute important
 inputs to the Tb simulations.

The expected Tb error, i.e. the total of the MAP residual Tb error
 variance estimates (σ_m^2 , σ_s^2) and the Tb spread introduced by the posterior
 parameter uncertainties ($EnSp_{i,m,par}$, $EnSp_{i,s,par}$), is found to be consistent
 with the actual RMSD of 3 and 2.5 K for the long-term posterior Tb aver-
 ages and standard deviations. In other words, the joint estimation of RTM-
 parameters, σ_m and σ_s with DREAM_(ZS) results in a balance between actual
 and expected errors in Tb simulations, and in statistically adequate param-
 eter values and uncertainty estimates.

In summary, the Bayesian inference of the posterior distribution of the
 RTM-parameters ensures reliable Tb simulations with GEOS-5. Further-
 more, the DREAM_(ZS) algorithm also reveals the importance of observation
 error and simulation error that cannot be explained by the RTM parameters.
 These error sources can be addressed using model refinement and assimilation
 of satellite-observed Tb data.

1 Acknowledgement

2 The authors thank Yann Kerr and Ali Mahmoodi for their help with the
3 SMOS data.

5 References

- 6 Balsamo, G., J, F. M., Bélair, S., Deblonde, G., 2006. A global root-zone
7 soil moisture analysis using simulated L-band brightness temperature in
8 preparation for the hydros satellite mission. *Journal of Hydrometeorology*
9 7, 1126–1146.
- 10 CESBIO, IPSL, INRA, Reading University, Tor Vergata University, 2011.
11 SMOS level 2 processor for soil moisture. Tech. rep., CEBIO, IPLS-Service
12 d’Aeronomie, INRA-EPHYSE, Reading University, Tor Vergata Univer-
13 sity.
- 14 Choudhury, B. J., Schmugge, T. J., Chang, A., Newton, R. W., 1979. Ef-
15 fect of surface roughness on the microwave emission from soils. *Journal of*
16 *Geophysical Research* 84 (C9), 5699–5706.
- 17 Crosson, W., Limaye, A., Laymon, C., 2005. Parameter sensitivity of soil
18 moisture retrievals from airborne L-band radiometer measurements in
19 SMEX02. *IEEE Transactions on Geoscience and Remote Sensing* 43, 1517–
20 1528.
- 21 De Lannoy, G., Reichle, R., Pauwels, V., 2013. Global calibration of the
22 GEOS-5 L-band microwave radiative transfer model over non-frozen land

1 using SMOS observations. *Journal of Hydrometeorology* 14, 765–785,
2 <http://dx.doi.org/10.1175/JHM-D-12-092.1>.

3 De Lannoy, G. J. M., Houser, P. R., Pauwels, V. R. N., Verhoest, N. E. C.,
4 2006. Assessment of model uncertainty for soil moisture through ensemble
5 verification. *Journal of Geophysical Research* 111 (D10), D10101.1–18,
6 doi:10.1029/2005JD006367.

7 de Rosnay, P., Calvet, J., Kerr, Y., Wigneron, J., Lematre, F., Escorihuela,
8 M., Muñoz-Sabater, J., Saleh, K., Barri, J., Bouhours, G., Coret,
9 L., Cherel, G., Dedieu, G., Durbe, R., Fritz, N., Froissard, F., Hoedjes, J.,
10 Kruszkowski, A., Lavenu, F., Suquia, D., Waldteufel, P., 2006. SMOSREX:
11 A long term field campaign experiment for soil moisture and land surface
12 processes remote sensing. *Remote Sensing of Environment* 102, 377–389,
13 doi:10.1016/j.rse.2006.02.021.

14 de Rosnay, P., Drusch, M., Boone, A., Balsamo, G., Decharme, B., Harris,
15 P., Kerr, Y., Pellarin, T., Polcher, J., Wigneron, J., 2009. AMMA land
16 surface model intercomparison experiment coupled to the Community Microwave
17 Emission Model: ALMIP-MEM. *Journal of Geophysical Research*
18 114 (D05108), 1–18, doi:10.1029/2008JD010724.

19 Dobson, M., Ulaby, F., Hallikainen, M., El-Rayes, M. A., 1985. Microwave
20 dielectric behavior of wet soil - part II: Dielectric mixing models. *IEEE
21 Transactions on Geoscience and Remote Sensing* 23, 35–46.

22 Drusch, M., Holmes, T., de Rosnay, P., Balsamo, G., 2009. Comparing ERA-
23 40-based L-band brightness temperatures with Skylab observations: A

1 calibration/validation study using the Community Microwave Emission
2 Model. *Journal of Hydrometeorology* 10, 213–226.

3 Entekhabi, D., Njoku, E. G., O'Neill, P. E., Kellogg, K. H., Crow, W. T.,
4 Edelstein, W. N., Entin, J. K., Goodman, S. D., Jackson, T. J., Johnson,
5 J., Kimball, J., Piepmeier, J. R., Koster, R. D., Martin, N., McDonald,
6 K. C., Moghaddam, M., Moran, S., Reichle, R., Shi, J. C., Spencer, M. W.,
7 Thurman, S. W., Tsang, L., Van Zyl, J., 2010. The Soil Moisture Active
8 and Passive (SMAP) mission. *Proceedings of the IEEE* 98 (5), 704–716.

9 Gelman, A., Rubin, D., 1992. Inference from iterative simulation using mul-
10 tiple sequences. *Stat. Sci.* 7, 457–472.

11 Grant, J., Wigneron, J., Van de Griend, A. A., Kruszewski, A., Sobjaerg,
12 S. S., Skou, N., 2007. A field experiment on microwave forest radiometry:
13 L-band signal behaviour for varying conditions of surface wetness. *IEEE*
14 *Transactions on Geoscience and Remote Sensing* 109, 10–19.

15 Jackson, T., Schmugge, T. J., 1991. Vegetation effects on the microwave
16 emission of soils. *Remote Sensing of Environment* 36, 203–212.

17 Kennedy, J., Eberhart, R., 1995. Particle swarm optimization. In: *Proc. Int.*
18 *Conf. Neur. Netw.* Piscataway, NJ.

19 Kerr, Y., Waldteufel, P., Wigneron, J.-P., Delwart, S., Cabot, F., Boutin, J.,
20 Escorihuela, M.-J., Font, J., Reul, N., Gruhier, C., Juglea, S., Drinkwa-
21 ter, M., Hahne, A., Martin-Neira, M., Mecklenburg, S., 2010. The SMOS
22 mission: New tool for monitoring key elements of the global water cycle.
23 *Proceedings of the IEEE* 98 (5), 666–687.

- 1 Kerr, Y. H., Njoku, E. G., 1990. A semiempirical model for interpreting
2 microwave emission from semiarid land surfaces as seen from space. IEEE
3 Transactions on Geoscience and Remote Sensing 28 (3), 384–393.
- 4 Kerr, Y. H., Waldteufel, P., Richaume, P., Wigneron, J. P., Ferrazzoli, P.,
5 Mahmoodi, A., Al Bitar, A., Cabot, F., Gruhier, C., Juglea, S. E., Ler-
6 oux, D., Mialon, A., Delwart, S., 2012. The SMOS soil moisture retrieval
7 algorithm. IEEE Transactions on Geoscience and Remote Sensing 50 (5),
8 1384–1403.
- 9 Konings, A., Entekhabi, E., Chan, S. K., Njoku, E. G., 2011. The effect of
10 rtm-parameter on satellite-based soil moisture retrievals. IEEE Transac-
11 tions on Geoscience and Remote Sensing 49, 2686–2698.
- 12 Koster, R. D., Suarez, M. J., Ducharne, A., Stieglitz, M., Kumar, P., 2000.
13 A catchment-based approach to modeling land surface processes in a gen-
14 eral circulation model 1. model structure. Journal of Geophysical Research
15 105 (D20), 24809–24822.
- 16 Laloy, E., Vrugt, J., 2012. High-dimensional posterior exploration
17 of hydrologic models using multiple-try DREAM₊(ZS) and high-
18 performance computing. Water Resources Research 48 (W01526),
19 doi:10.1029/2011WR010608.
- 20 Loveland, T. R., Belward, A. S., 1997. The IGBP-DIS global 1-km land cover
21 data set, DIScover: first results. International Journal of Remote Sensing
22 65, 1031–1031.

- 1 Mironov, V., Dobson, M., Kaupp, V., Komarov, S., Kleshchenko, V., 2004.
2 Generalized refractive mixing dielectric model for moist soil. IEEE Trans-
3 actions on Geoscience and Remote Sensing 42, 773–785.
- 4 O’Neill, P., Njoku, E., Jackson, T., Chan, S., Bindlish, R., 2012. SMAP
5 Algorithm Theoretical Basis Document: L2 & L3 soil moisture (passive)
6 products. Tech. Rep. SMAP Project, JPL D-66481, Jet Propulsion Labo-
7 ratory, Pasadena, CA.
- 8 Panciera, R., Walker, J. P., Merlin, O., 2009. Improved understanding of
9 soil surface roughness parameterization for L-band passive microwave soil
10 moisture retrieval. IEEE Transactions on Geoscience and Remote Sensing
11 6 (4), 625–629.
- 12 Parinussa, R. M., Meesters, A. G., Liu, Y. Y., Dorigo, W., Wagner, W.,
13 de Jeu, R. A., 2011. Error estimates for near-real-time satellite soil mois-
14 ture as derived from the land parameter retrieval model. IEEE Transac-
15 tions on Geoscience and Remote Sensing 8 (4), 779–783.
- 16 Pellarin, T., Wigneron, J., Calvet, J., Berger, M., Douville, H., Ferrazzoli, P.,
17 Kerr, Y. H., Lopez-Baeza, E., Pulliainen, J., Simmonds, L. P., Waldteufel,
18 P., 2003. Two-year global simulation of L-band brightness temperatures
19 over land. IEEE Transactions on Geoscience and Remote Sensing 42 (9),
20 2135–2139.
- 21 Reichle, R., Crow, W., Koster, R., Kimball, J., De Lannoy, G., 2012. SMAP
22 Algorithm Theoretical Basis Document: L4 surface and root zone soil

1 moisture product. Tech. Rep. SMAP Project, JPL D-66483, Jet Propulsion
2 Laboratory, Pasadena, CA.

3 Reichle, R. H., 2012. The MERRA-land data product (version 1.2), GMAO
4 office note No. 3. Tech. rep., NASA Global Modeling and Assimilation
5 Office, available at http://gmao.gsfc.nasa.gov/pubs/office_notes/.

6 Reichle, R. H., Koster, R. D., De Lannoy, G. J. M., Forman, B. A., Liu,
7 Q., Mahanama, S. P. P., Toure, A., 2011. Assessment and enhancement of
8 MERRA land surface hydrology estimates. *Journal of Climate* 24, 6322–
9 6338.

10 Reichle, R. H., Walker, J. P., Koster, R. D., Houser, P. R., 2002. Extended
11 vs. ensemble kalman filtering for land data assimilation. *Journal of Hy-*
12 *drometeorology* 3, 728–740.

13 Rienecker, M. M., Suarez, M. J., Gelaro, R., Todling, R., Bacmeister, J., Liu,
14 E., Bosilovich, M. G., Schubert, S. D., Takacs, L., Kim, G.-K., Bloom, S.,
15 Chen, J., Collins, D., Conaty, A., da Silva, A., Gu, W., Joiner, J., Koster,
16 R. D., Lucchesi, R., Molod, A., Owens, T., Pawson, S., Pegion, P., Red-
17 der, C. R., Reichle, R., Robertson, F. R., Ruddick, A. G., Sienkiewicz,
18 M., Woollen, J., 2011. MERRA - NASA’s modern-era retrospective anal-
19 ysis for research and applications. *Journal of Climate* 24 (14), 3624–3648,
20 doi:10.1175/JCLI-D-11-00015.

21 Sabater, J. M., de Rosnay, P., Balsamo, G., 2011. Sensitivity of L-band
22 NWP forward modelling to soil roughness. *International Journal of Remote*
23 *Sensing iFirst*, 1–14, doi:10.1080/01431161.2010.507260.

- 1 Vrugt, J., Sadegh, M., 2013. Towards diagnostic model calibration and eval-
2 uation: Approximate Bayesian Computation. *Water Resources Research*
3 49, doi: 10.1002/wrcr.20354.
- 4 Vrugt, J., ter Braak, C., Clark, M., Hyman, J., Robinson, B., 2008. Treat-
5 ment of input uncertainty in hydrologic modeling: Doing hydrology back-
6 ward with Markov chain Monte Carlo simulation. *Water Resources Re-*
7 *search* 44 (W00B09), doi:10.1029/2007WR006720.
- 8 Vrugt, J. A., ter Braak, C., Diks, C., Robinson, B. A., Hyman, J. M., Higdon,
9 D., 2009. Accelerating Markov chain Monte Carlo simulation by differential
10 evolution with self-adaptive randomized subspace sampling. *International*
11 *Journal of Nonlinear Sciences & Numerical Simulation* 10 (3), 271–288.
- 12 Wang, J. R., Choudhury, B. J., 1981. Remote sensing of soil moisture content
13 over bare field at 1.4 GHz frequency. *Journal of Geophysical Research* 86,
14 5277–5282.
- 15 Wang, J. R., Schmugge, T. J., 1980. An empirical model for the complex
16 dielectric permittivity of soils as a function of water content. *IEEE Trans-*
17 *actions on Geoscience and Remote Sensing* GE-18 (4), 288–295.
- 18 Wöhling, T., Vrugt, J. A., 2011. Multiresponse multilayer vadose zone model
19 calibration using Markov chain Monte Carlo simulation and field water
20 retention data. *Water Resources Research* 47, W04510.1–19.

1 Appendix A. Radiative Transfer Model

2 A diagnostic zero-order (tau-omega) microwave RTM is used to simulate
 3 L-band Tb at the top of the atmosphere ($Tb_{TOA,p}$ [K]). The $Tb_{TOA,p}$ at
 4 polarization $p = [H, V]$ (horizontal or vertical) is a combination of (i) soil
 5 emission, possibly attenuated by vegetation, (ii) vegetation emission, possibly
 6 reflected by the soil, and (iii) atmospheric effects:

$$\begin{aligned} Tb_{TOV,p} = & T_s(1 - r_p)A_p + T_c(1 - \omega_p)(1 - A_p)(1 + r_pA_p) \\ & + Tb_{ad,p}r_pA_p^2 \end{aligned} \quad (A.1)$$

$$Tb_{TOA,p} = Tb_{au,p} + \exp(-\tau_{atm,p})Tb_{TOV,p} \quad (A.2)$$

7 where $Tb_{TOV,p}$ [K] is the top of vegetation Tb, T_s [K] is the surface soil tem-
 8 perature, T_c [K] is the canopy temperature (assumed equal to T_s), $Tb_{ad,p}$ [K]
 9 and $Tb_{au,p}$ [K] are the downward and upward atmospheric radiation, A_p [-] is
 10 the vegetation attenuation, $\exp(-\tau_{atm,p})$ [-] is the atmospheric attenuation,
 11 $\tau_{atm,p}$ [-] is the atmospheric optical depth, r_p [-] is the rough surface reflec-
 12 tivity, and ω_p [-] is the scattering albedo. The atmospheric contributions
 13 ($Tb_{ad,p}$, $Tb_{au,p}$ and $\exp(-\tau_{atm,p})$) are described by Pellarin et al. (2003). The
 14 rough surface reflectivity r_p [-] is derived from the smooth surface reflectivity
 15 R_p [-] following (Choudhury et al., 1979; Wang and Choudhury, 1981):

$$r_p = (Q R_q + (1 - Q)R_p) \exp(-h) \cos^{Nr_p}(\theta) \quad (A.3)$$

16 where Q [-] is the polarization mixing ratio and typically set to 0 for L-
 17 band (Kerr and Njoku, 1990), θ [rad] is the incidence angle, h [-] is the
 18 roughness parameter accounting for dielectric properties that vary at the sub-
 19 wavelength scale, Nr_p [-] is the angular dependence, and $q = V$ for $p = H$

1 and vice versa. The smooth surface reflectivity R_p [-] is given by the Fresnel
2 equations as a function of the dielectric constant, which itself depends on soil
3 moisture, temperature, texture, incidence angle and wavelength. We select
4 the Wang and Schmugge (1980) soil dielectric mixing model for this study.
5 The results with this model are similar to what is obtained with the Mironov
6 et al. (2004) model, and both are in a better agreement with the SMOS data
7 than the Dobson et al. (1985) model. We include the dependence of h on soil
8 moisture (SM [$m^3.m^{-3}$]) through a stepwise linear expression (adapted from
9 the proposed SMOS soil moisture retrieval algorithm (CESBIO et al., 2011;
10 Kerr et al., 2012)):

$$h = \begin{cases} h_{max} & \text{if } SM \leq wt \\ h_{max} + \frac{h_{min}-h_{max}}{poros-wt} (SM - wt) & \text{if } wt < SM \leq poros \end{cases} \quad (A.4)$$

11 where $poros$ [$m^3.m^{-3}$] and wt [$m^3.m^{-3}$] are the porosity and transition soil
12 moisture, respectively. The latter is modeled as $wt = 0.48.wp + 0.165$ (Wang
13 and Schmugge (1980)) where wp [$m^3.m^{-3}$] is the wilting point.

14 The vegetation attenuation A_p [-] is based on the Jackson and Schmugge
15 (1991) vegetation opacity model:

$$A_p = \exp\left(-\frac{\tau_p}{\cos \theta}\right), \text{ with} \quad (A.5)$$

$$\tau_p = b_p VWC = b_p LEWT LAI \quad (A.6)$$

16 where τ_p [-] is the nadir vegetation opacity, which is a function of a vegetation
17 structure parameter b_p [-] and the vegetation water content (VWC) [$kg.m^{-2}$].
18 The latter is modeled here as the product of LAI [$m^2.m^{-2}$] and the leaf
19 equivalent water thickness ($LEWT$) [$kg.m^{-2}$].

1 List of Tables

2	1	Parameters selected for calibration in different scenarios (P,	
3		D, D_σ) with an indication of the allowed parameter range and	
4		the prior estimate for each IGBP vegetation class within the	
5		study domain. $\Delta h \equiv h_{max} - h_{min}$, $\Delta b \equiv b_V - b_H$	40
6	2	Domain-averaged parameters values and their uncertainty <i>stdv</i> [.]	
7		for the prior distributions and the posterior distributions ob-	
8		tained with scenarios P, D and D_σ . The bottom half of the	
9		table shows ensemble Tb prediction statistics (square-root of	
10		Eq. 7-8, 9-10 and 11-12), averaged across 24 long-term Tb ob-	
11		servations and calculated for the calibration period. Only for	
12		the prior parameters, σ_m and σ_s are calculated assuming (a)	
13		$RME nSp_m = RMSD_{\overline{m}}$ and $RME nSp_s = RMSD_{\overline{s}}$, and (b)	
14		$\sigma_m = \sqrt{RMSD_{\overline{m}}^2 - RME nSp_{m,par}^2}$ and $\sigma_s = \sqrt{RMSD_{\overline{s}}^2 - RME nSp_{s,par}^2}$.	
15		41	

1 List of Figures

2	1	Study domain with indication of the dominant IGBP vegeta-	
3		tion classes.	42
4	2	Illustration of marginal distributions for (a) RTM-parameters	
5		and (b) Tb simulations at a single grid cell. Crosses (\times) indi-	
6		cate the MAP estimates, the vertical dashed lines and white	
7		box indicate the ensemble mean posterior estimate, and hor-	
8		izontal dotted arrows indicate one standard deviation uncer-	
9		tainty around the ensemble mean. The performance of the	
10		Tb simulations is quantified by comparing either the MAP	
11		$(m_i(\boldsymbol{\alpha}_{MAP}), s_i(\boldsymbol{\alpha}_{MAP}))$ or the ensemble mean $(\overline{m_i(\boldsymbol{\alpha})}, \overline{s_i(\boldsymbol{\alpha})})$	
12		simulations against (black dots) 24 observed values $(m_{i,o}, s_{i,o})$	
13		with $i = 1, \dots, 24$. The differences Δ_{m_i} and $\Delta_{\overline{m_i}}$ contribute	
14		to MSD_m (Eq. 5) and $MSD_{\overline{m}}$ (Eq. 7), respectively.	43
15	3	Parameter values for (left) $\langle h \rangle$, (middle) $\langle \tau \rangle$, and (right)	
16		ω , for the (top row) prior distribution and scenarios (second	
17		row) P, (third row) D and (fourth row) D_σ	44
18	4	Uncertainty in parameter estimates for (left) $\langle h \rangle$, (middle)	
19		$\langle \tau \rangle$, and (right) ω , obtained with DREAM _(ZS) scenario (top	
20		row) D and (bottom row) D_σ	45
21	5	(Left) MAP parameter values and (right) uncertainties aggre-	
22		gated per vegetation class for DREAM _(ZS) scenarios D and D_σ .	
23		Each row represents a different parameter: (a,b) $\langle h \rangle$, (c,d)	
24		τ , (e,f) ω , (g,h) σ_m , (i,j) σ_s	46

1	6	RMSD in long-term Tb (a,c) average and (b,d) standard deviation during the (top) calibration (1 July 2011 - 1 July 2012) and (bottom) evaluation period (1 July 2010 - 1 July 2011), using the MAP parameter values derived from PSO (scenario P) and DREAM _(ZS) (scenarios D and D _{σ}).	47
6	7	(a-b) Long-term average and (c-d) standard deviation, for (a-c) H- and (b-d) V-polarized Tb (dots) SMOS observations and (lines) ensemble simulations averaged over the study domain, during the calibration period (1 July 2011 - 1 July 2012) and only including ascending time steps. The simulations use an ensemble of parameter estimates derived with DREAM _(ZS) scenarios (gray) D and (black) D _{σ} . The ensemble mean is shown by a central horizontal dash. The error bars indicate the total simulation and observation uncertainty and are drawn around the simulated Tb for illustration. For clarity, symbols are slightly offset from the nominal incidence angle.	48
17	8	Gelman-Rubin convergence diagnostic \sqrt{R} for the two DREAM _(ZS) MCMC simulation scenarios. The metric is averaged over all calibrated parameters, and across the study domain.	49

Table 1: Parameters selected for calibration in different scenarios (P, D, D $_{\sigma}$) with an indication of the allowed parameter range and the prior estimate for each IGBP vegetation class within the study domain. $\Delta h \equiv h_{max} - h_{min}$, $\Delta b \equiv b_V - b_H$.

	h_{min} [-]	Δh [-]	ω [-]	b_H [-]	Δb [-]	σ_m [K]	σ_s [K]
P, D	X	X	X	X	X	-	-
D $_{\sigma}$	X	X	X	X	X	X	X
α_{min}	0	0	0	0	-0.15	1E-5	1E-5
α_{max}	2.0	1.0	0.3	0.7	0.15	60	40
ENF Evergreen Needleleaf Forest	1.2	0	0.05	0.33	0	1	1
DBF Deciduous Broadleaf Forest	1	0	0.05	0.33	0	1	1
MXF Mixed Forest	1.3	0	0.05	0.33	0	1	1
CSH Closed Shrublands	0.7	0	0.05	0.3	0	1	1
OSH Open Shrublands	0.7	0	0.05	0.3	0	1	1
WSV Woody Savannas	0.7	0	0.05	0.3	0	1	1
GRS Grasslands	0.1	0	0.05	0.2	0	1	1
CRP Croplands	0.5	0	0.05	0.15	0	1	1
CRN Crop and Natural Vegetation	0.7	0	0.05	0.15	0	1	1

Table 2: Domain-averaged parameters values and their uncertainty $stdv[.]$ for the prior distributions and the posterior distributions obtained with scenarios P, D and D_σ . The bottom half of the table shows ensemble Tb prediction statistics (square-root of Eq. 7-8, 9-10 and 11-12), averaged across 24 long-term Tb observations and calculated for the calibration period. Only for the prior parameters, σ_m and σ_s are calculated assuming (a) $RMEnSp_m = RMSD_{\overline{m}}$ and $RMEnSp_s = RMSD_{\overline{s}}$, and (b) $\sigma_m = \sqrt{RMSD_{\overline{m}}^2 - RMEnSp_{m,par}^2}$ and $\sigma_s = \sqrt{RMSD_{\overline{s}}^2 - RMEnSp_{s,par}^2}$.

	Prior	P	D	D_σ
$\langle h \rangle [-]$	0.59	0.74	0.75	0.77
$\langle \tau \rangle [-]$	0.35	0.26	0.26	0.25
$\omega [-]$	0.05	0.09	0.09	0.09
σ_m [K]	7.45 ^b	1.00	1.00	3.08
σ_s [K]	4.78 ^b	1.00	1.00	2.39
$stdv[\langle h \rangle] [-]$	0.63	-	0.04	0.10
$stdv[\langle \tau \rangle] [-]$	0.27	-	0.02	0.04
$stdv[\omega] [-]$	0.09	-	0.01	0.02
$stdv[\sigma_m]$ [K]	-	-	-	0.71
$stdv[\sigma_s]$ [K]	-	-	-	0.53
$RMSD_{\overline{m}}$ [K]	7.63	-	2.77	3.02
$RMSD_{\overline{s}}$ [K]	5.04	-	2.53	2.54
$RMEnSp_m$ [K]	7.63 ^a	-	1.04	3.24
$RMEnSp_s$ [K]	5.04 ^a	-	1.01	2.45
$RMEnSp_{m,par}$ [K]	1.65	-	0.28	0.92
$RMEnSp_{s,par}$ [K]	1.57	-	0.14	0.39

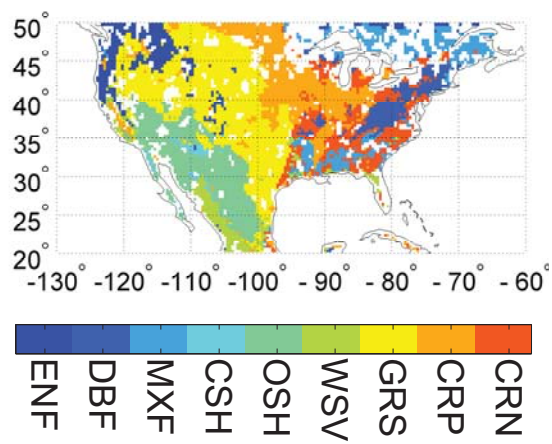


Figure 1: Study domain with indication of the dominant IGBP vegetation classes.

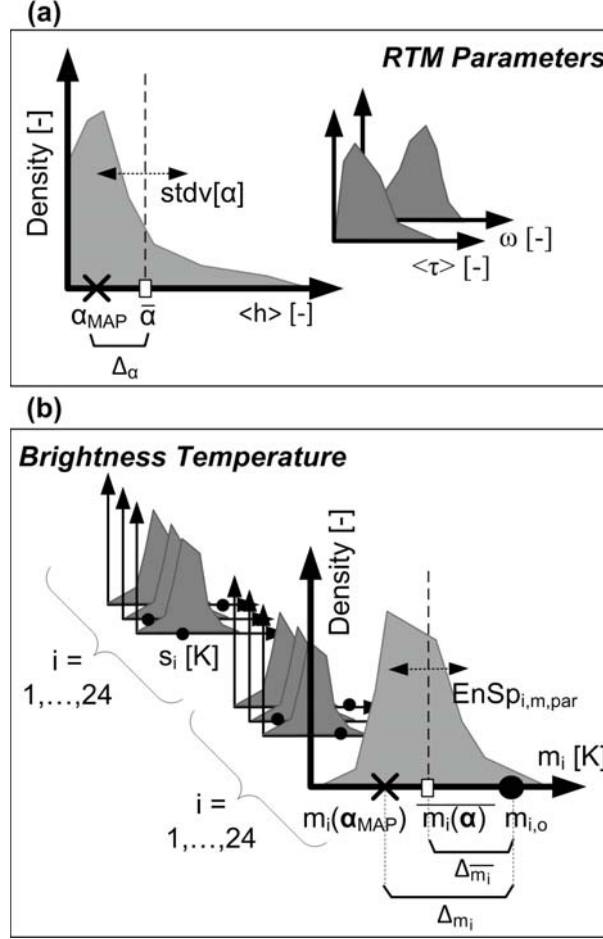


Figure 2: Illustration of marginal distributions for (a) RTM-parameters and (b) Tb simulations at a single grid cell. Crosses (\times) indicate the MAP estimates, the vertical dashed lines and white box indicate the ensemble mean posterior estimate, and horizontal dotted arrows indicate one standard deviation uncertainty around the ensemble mean. The performance of the Tb simulations is quantified by comparing either the MAP ($m_i(\alpha_{MAP})$, $s_i(\alpha_{MAP})$) or the ensemble mean ($\bar{m}_i(\alpha)$, $\bar{s}_i(\alpha)$) simulations against (black dots) 24 observed values ($m_{i,o}$, $s_{i,o}$) with $i = 1, \dots, 24$. The differences Δ_{m_i} and $\Delta_{\bar{m}_i}$ contribute to MSD_m (Eq. 5) and $MSD_{\bar{m}}$ (Eq. 7), respectively.

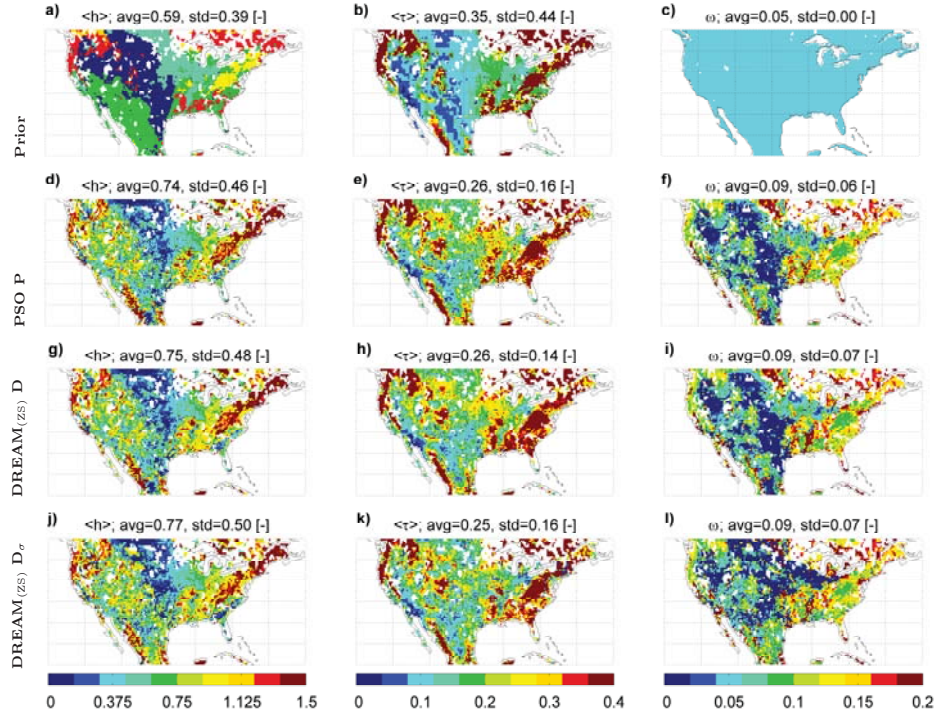


Figure 3: Parameter values for (left) $\langle h \rangle$, (middle) $\langle \tau \rangle$, and (right) ω , for the (top row) prior distribution and scenarios (second row) P, (third row) D and (fourth row) D_σ.

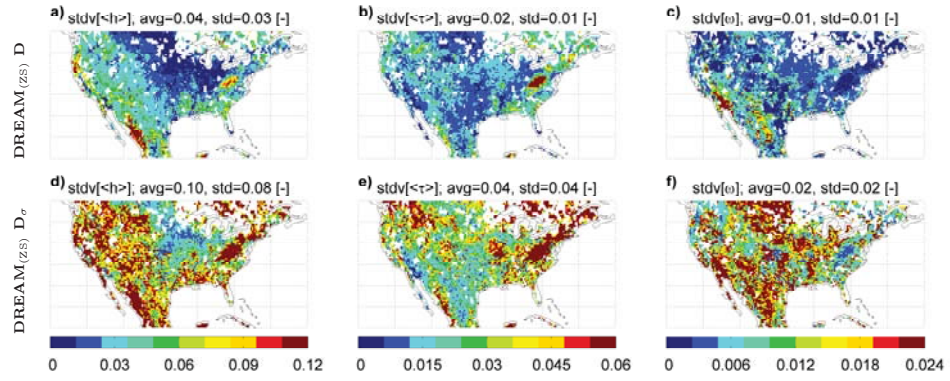


Figure 4: Uncertainty in parameter estimates for (left) $\langle h \rangle$, (middle) $\langle \tau \rangle$, and (right) ω , obtained with DREAM_(ZS) scenario (top row) D and (bottom row) D_σ.

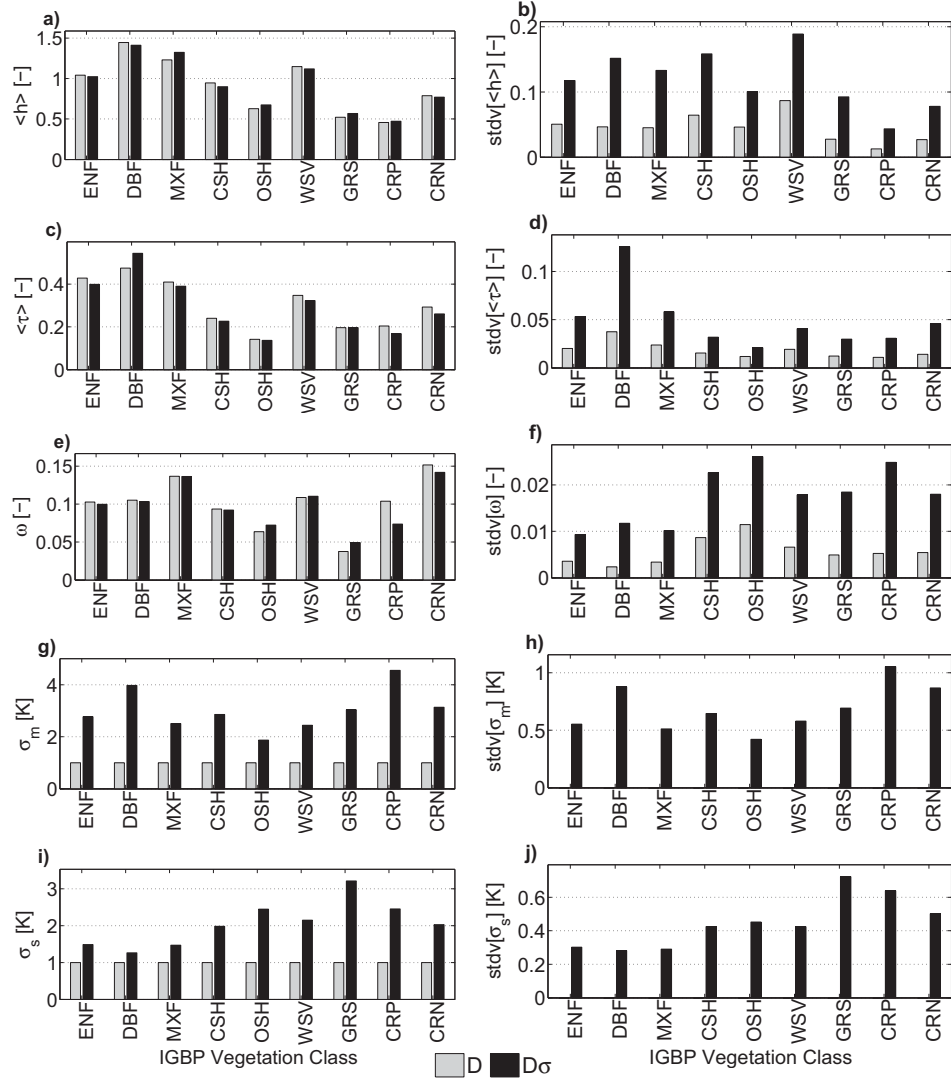


Figure 5: (Left) MAP parameter values and (right) uncertainties aggregated per vegetation class for DREAM_(ZS) scenarios D and D σ . Each row represents a different parameter: (a,b) $\langle h \rangle$, (c,d) τ , (e,f) ω , (g,h) σ_m , (i,j) σ_s .

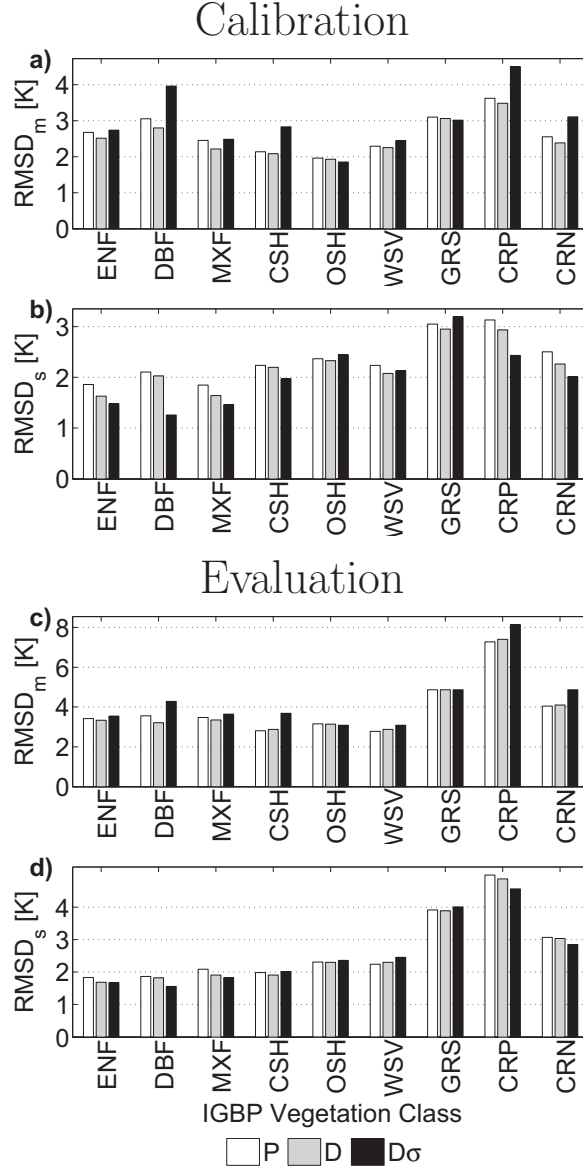


Figure 6: RMSD in long-term Tb (a,c) average and (b,d) standard deviation during the (top) calibration (1 July 2011 - 1 July 2012) and (bottom) evaluation period (1 July 2010 - 1 July 2011), using the MAP parameter values derived from PSO (scenario P) and DREAM_(ZS) (scenarios D and D σ).

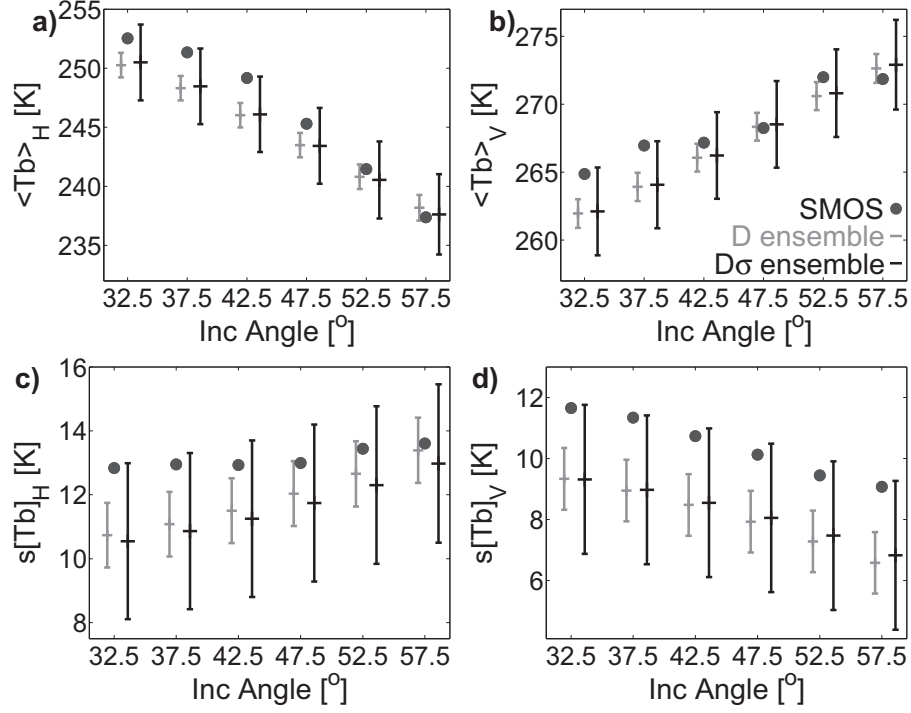


Figure 7: (a-b) Long-term average and (c-d) standard deviation, for (a-c) H- and (b-d) V-polarized Tb (dots) SMOS observations and (lines) ensemble simulations averaged over the study domain, during the calibration period (1 July 2011 - 1 July 2012) and only including ascending time steps. The simulations use an ensemble of parameter estimates derived with DREAM_(ZS) scenarios (gray) D and (black) D σ . The ensemble mean is shown by a central horizontal dash. The error bars indicate the total simulation and observation uncertainty and are drawn around the simulated Tb for illustration. For clarity, symbols are slightly offset from the nominal incidence angle.

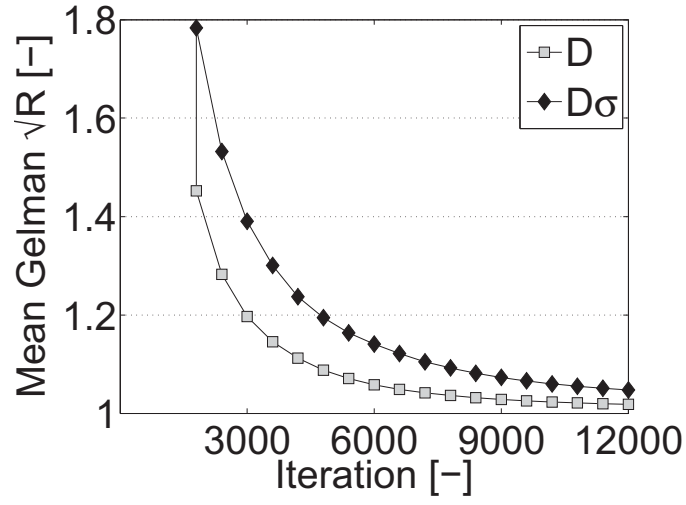


Figure 8: Gelman-Rubin convergence diagnostic \sqrt{R} for the two DREAM_(zs) MCMC simulation scenarios. The metric is averaged over all calibrated parameters, and across the study domain.